Materials Science & Engineering A 649 (2016) 39–47

Contents lists available at ScienceDirect

Materials Science & Engineering A

journal homepage: www.elsevier.com/locate/msea

Local deformation mechanisms of two-phase Ti alloy

Tea-Sung Jun*, Giorgio Sernicola, Fionn P.E. Dunne, T. Benjamin Britton

Department of Materials, Royal School of Mines, Imperial College London, London SW7 2AZ, UK

ARTICLE INFO

Article history:
Received 23 June 2015
Received in revised form
3 September 2015
Accepted 3 September 2015
Available online 25 September 2015

Keywords:
Micropillar compression
Two-phase Ti alloys
EBSD
Micromechanics

ABSTRACT

This paper describes a study of local deformation mechanisms in two-phase Ti alloy, Ti–6Al–2Sn–4Zr–2Mo, by performing *in-situ* micropillar compression tests. A colony microstructure was examined and select grains identified for examination were chosen with EBSD measurements. These grains were chosen to isolate individual slip systems within each test. Micropillars of tri-crystal (α–β–α) structure were fabricated from four determined regions, and compression tests were performed using a displacement-controlled nanoindenter set inside a SEM, with a constant displacement rate. The results show that the α/β morphology significantly affects the local deformation behaviour. For these colony structures, Schmid's law in general enables anticipation of local slip activity, but the presence and morphology of the β phase can significantly alter the apparent yielding point and work hardening response. The role of interfaces within these tri-crystal pillars is discussed.

1. Introduction

High strength-to-weight ratio, corrosion resistance and excellent mechanical properties have made titanium alloys attractive to many industrial applications, particularly in gas turbine and aerostructures. However, their highly anisotropic and localised deformation behaviour, when significant fractions of the α (Hexagonal Close Packed, HCP) phase are present, lead to difficulties in understanding fatigue crack nucleation and hence in predicting lifetime and failure of components in service [1]. In the last few decades, extensive researches have been devoted to understanding deformation mechanisms in α phase titanium (e.g., CP–Ti or Ti–Al single crystals) [2–7]. These investigations have clearly shown slip/twinning behaviours and the corresponding dislocation evaluation as a function of Al content, temperature and crystallographic orientation. On the other hand, relatively little is known about the precise micromechanical deformation mechanisms in two-phase Ti alloys. Complexities on studying α/β Ti alloys arise due to the microstructure-dependent-mechanical properties, room temperature creep behaviour, microtexture and interaction between the α and β (Body Centred Cubic, BCC) phases [8–12].

Early work by Chan et al. [8] showed the deformation behaviour of a colony-structured α/β Ti alloy, Ti–8Al–1Mo–1V. Compression experiments of individual colony samples revealed that significant yield stress variations were found with respect to the angle between the slip direction and the normal to the α/β interface, and failure of Schmid's law was observed in α colony orientations where angles between the slip plane normal and the loading direction vary from 15° to 63°, except the case when slip occurred parallel to the β phase. Slip system activity strongly influences stress–strain behaviour and interestingly the authors insisted based on experimental observation that the β phase is stronger than the α phase, although this has not yet been confirmed.

Savage et al. [11] and Suri et al. [12] investigated the effects of α/β interfaces in Ti–6Al–2Sn–4Zr–2Mo–0.1Si and Ti–5Al–2.5Sn–0.5Fe, respectively, with respect to slip transmission mechanisms between the α and β phases governed by Burgers orientation relationship (BOR). Experimental observation revealed that significant anisotropy in deformation behaviour occurs in three distinctive (a_1, a_2 and a_3) basal and prismatic slip systems in the α phase which was caused by the relative misalignment with a slip system in the β phase. The morphological effect of the β phase in deformation was studied by Sandala [10] using lamellar structured Ti–6Al–2Sn–4Zr–6Mo with different widths of β. It revealed that the β width significantly affects plastic deformation behaviour, whilst no pronounced effect was found in the elastic regime. Some effects of β volume fraction can be found in recent work done by Qiu et al. [9]. With a higher β volume fraction obtained by increasing Mo content in Ti–6Al–2Sn–4Zr–*x*Mo (x=2–6), a smaller slip band spacing was produced and significantly reduced accumulated strains were observed during dwell fatigue tests.

Previous studies have shown some aspects of deformation mechanisms in macroscopic polycrystalline two-phase Ti alloy samples, but it is thought that small-scale experiments on a

* Corresponding author.
E-mail address: t.jun@imperial.ac.uk (T.-S. Jun).

http://dx.doi.org/10.1016/j.msea.2015.09.016
0921-5093/

localised, confined area are required to improve understanding of the fundamental mechanisms on the level of the individual microstructural constituents. In recent years, Uchic et al. [13] have developed an innovative methodology for studying micro-mechanical behaviour of materials by adopting experiments on small-scale architectures fabricated by focused ion beam, with a nanoindenter as a means of applying force. Extensive research contributions have been devoted to investigate the length scale and size effects in plasticity of metallic materials [13–17], yet this has mainly focused on FCC materials such as Cu and Ni. Some work on Ti single crystals has been carried out to study the size effect on slip [18] and deformation twinning [19]. Recently, Ding, Gong and colleagues [20] have worked on two-phase Ti–6Al–4V using micro-cantilevers, investigating slip activities through the α/β interface. They found a cross-slip away from the $\{10\bar{1}1\}$ pyramidal plane only for compression case (not for tension) and this could elucidate asymmetric CRSS behaviour, which was similarly observed by Jones and Hutchinson [21].

In this work, we investigate local deformation mechanisms in two-phase Ti alloys using micropillar compression focusing on how two phase structures change local slip behaviour. We investigate the significance of α/β structural morphology on deformation and its effect on Schmid's law, which is used for anticipating local slip activity. This work provides the basis for further investigation on fundamental micromechanics of two-phase Ti alloys and potentially other materials.

2. Materials and experiments

2.1. Material preparation

A titanium alloy 6242 (hereinafter referred to as Ti6242), with the chemical composition (in wt%): 6.12Al–2.00Sn–3.95Zr–2.00Mo–0.012C–0.031Fe–0.021Si–0.0002H–0.072O–0.0069N and Ti balance was supplied by IMR (Institute of Metal Research, China) as a forged bar of 20 mm diameter. The bar had been produced by a triple VAR melt, followed by β forging at the temperature of T_β (β transus)+150 °C with 30% deformation (resulting in the ingot diameter from 205–210 mm to 170 mm) and α/β forging at the temperature of 30% α_p (primary α phase) with 70% deformation giving a finishing diameter of 90 mm.

The sample was sectioned perpendicular to the bar axis and prepared metallographically with SiC papers (up to 4000 grit) and then polished with ~50 nm OP-S (Oxide Polishing Suspensions) diluted with H_2O by a ratio 1:5 of OP-S:H_2O. The sample was lightly etched with Kroll's reagent for ~15 s (2% HF, 10% HNO_3 and 88% H_2O). The final etch and polish procedure was repeated 2–3 times until the grain structure was clearly visible with polarised light microscopy.

Initial studies of the as-received Ti bars revealed complex lamellar structures, where isolation of individual microstructure features would be difficult and the effect of prior strain would make interpretation of the results difficult (see Fig 1). Therefore the sample was heat treated to produce a colony microstructure with large α-lamella separated by thin β-ligaments, in clear prior-β grain structures to make micropillars of a tri-crystal (α–β–α) structure (see Fig. 2(i)). For this heat treatment, the as-received sample was held at the temperature of β transus+50 °C (i.e., 1040 °C) for 8 h and cooled down with a rate of 1 °C/min. This provided a microstructure with α phase lamella, with average widths of ~3.7 μm, and β phase ligaments of width ~0.8 μm. Note that the widths of the as-received condition were ~2 μm for α lamella and ~0.5 μm for β ligament.

2.2. EBSD maps

Electron backscatter diffraction (EBSD) maps were generated in a Carl Zeiss Auriga CrossBeam FIB-SEM with Bruker EBSD system consisting of an eFlashHR camera and Esprit v1.9 software, in order to characterise the microstructure (an example is shown in Fig. 1). High current mode was used with a probe current of 10.5 nA and an aperture size of 120 μm. The accelerating voltage of 20 kV was selected for EBSD. A larger area map (~1.6 × 1.2 mm^2 and step size with 1.2 μm) was first mapped, yet due to the large step size the β orientation was not regularly revealed within this map. Therefore higher magnification maps (~151 × 113 μm^2) with finer step sizes of 0.05–0.5 μm were captured for areas with desired crystal orientations for the micropillar tests. Crystal orientations were selected to maximise the resolved shear stress on individual slip systems and trigger single slip.

2.3. Micropillar fabrication

Micropillars of square cross-section were machined using a FEI Helios Nanolab 600. An automated routine was used for fabrication in AutoScript™. A Ga^+ ion beam of 30 kV was used with a series of currents decreasing from 9.3 nA (rough milling) to 2.8 nA (medium milling) and finally to 0.92 nA (final milling). The fabrication time for each pillar was about 17 min.

Micropillars were fabricated in grains of specific crystallographic orientations to control slip activity. Furthermore, pillars

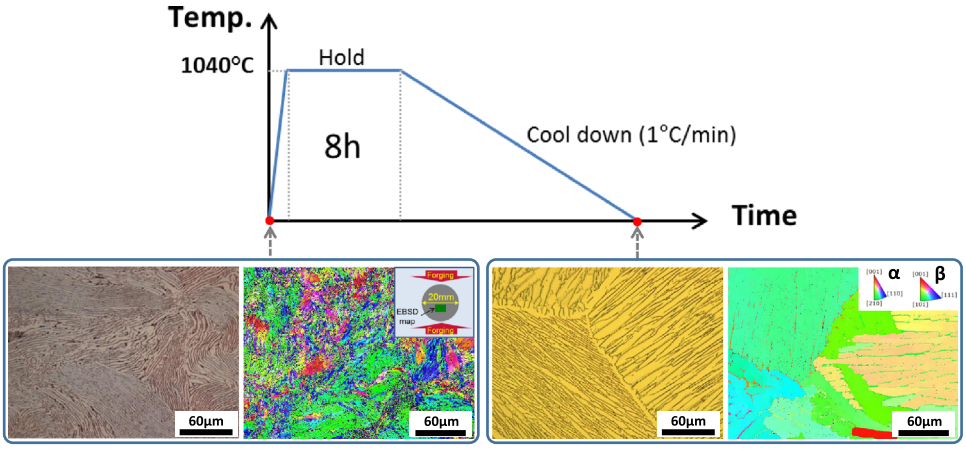

Fig. 1. Schematic diagram of heat treatment (HT) processing route, optical micrographs and EBSD inverse pole figure (IPF) maps observed with respect to normal to the forging direction, taken before and after HT: Sufficiently low cooling rate changed microstructure in as-received (before HT) Ti6242 to fully lamellar structure. All images were observed in different regions.

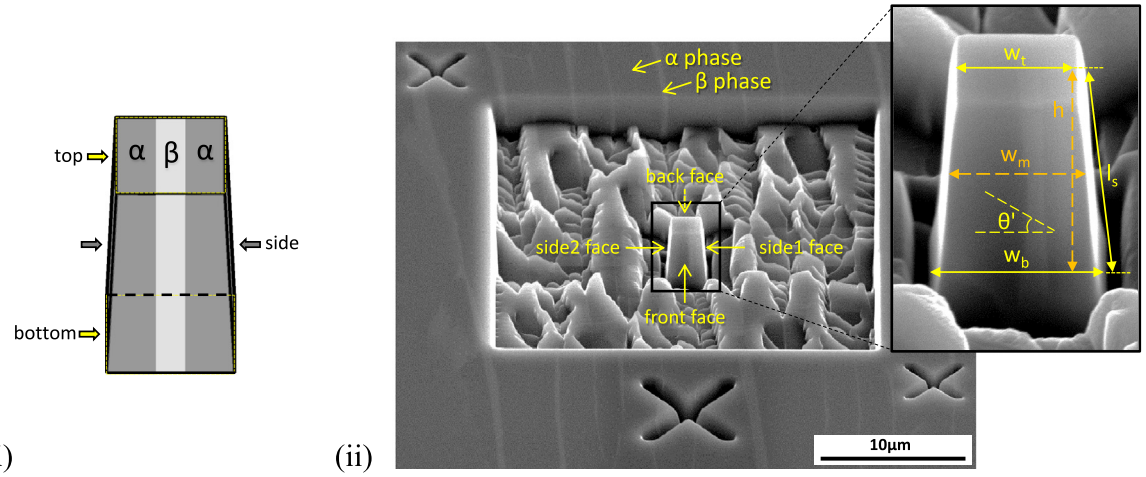

Fig. 2. (i) Schematic diagram of tri-crystal(α–β–α) structured micropillar and (ii) SEM image of a square-shape micropillar fabricated using focused ion beam with a script created by AutoScript™: α (darker) and β (brighter) phases are seen clearly on the pillar, and their orientation difference causes a surface stepping within a trench. Four faces shown in black rectangle are used for slip trace analysis. In sub-window, pillar height (h) and area (w_m^2) were used to calculate engineering strain and stress, respectively.

were fabricated with the β phase running near vertical in the pillar. Due to different crystallographic orientations of the α and β phases, anisotropic milling led to roughening between the phases [22].

Each pillar was carefully measured after fabrication (see Fig. 2 (ii)). The pillar widths (w_t and w_b) and the side length (l_s) were measured, where the taper angle (θ_t) and a height (h) are then defined by the following equations:

$$\theta_t = \sin^{-1}\left(\frac{w_b - w_t}{2l_s}\right) \text{ and } h = l_s \cos\theta_t \quad (1)$$

As the pillars are flat faced, slip trace analysis can be easily performed and the slip angle (θ_s) can be expressed as follows:

$$\theta_s = \tan^{-1}\left(\frac{\tan\theta'}{\sin\varphi}\right) \quad (2)$$

where θ' is an angle on any pillar faces after tilting and ϕ a tilting angle. Note that a tilting angle of 52° was predominantly used in this study. Among several micropillars fabricated, a total of nine pillars were selected for this study with a top width of 2 μm, an aspect ratio of 1.9:1–2.6:1, and a taper angle of 4.4–6.0°. The details of each pillar are summarised in Table 1.

2.4. Micropillar compression test

In-situ SEM based micropillar compression tests were performed using an Alemnis nanoindentation platform. This platform is actuated with a piezoelectric transducer and therefore operates in displacement control with up to maximum displacement of 35 μm and load of 500 mN. The samples were mounted on top of a calibrated load cell. The whole system was aligned to indent the pillars with a 30° tilt between sample and the horizontal plane. *In-situ* imaging was performed at a low working distance using the secondary electron (SE) detector with an accelerating voltage of 5 kV. The pillars were aligned such that tri-crystal phase was visible during the mechanical test. The indenter was loaded with a flat punch (10 μm diameter, set on top of a 60° cone).

The micropillars were near uniaxially compressed by the diamond flat punch tip at displacement rates of 2 and 5 nm s^{-1}, to a peak tip displacement of 1 μm. This is approximately strain rate of ~5×10^{-4} s^{-1} and ~1×10^{-3} s^{-1} respectively, assuming a uniform cross section. The punch was withdrawn, and held with 1/10th of the maximum displacement to measure thermal drift. This was used to correct the load–displacement results, although this correction was very small once the indenter was left to stabilise in the vacuum chamber (~2 h).

During each test, the SEM was used to generate an *in-situ* video of the surface, using a reduced window and an effective frame capture time of ~600 ms. These videos were synchronised with the load–displacement data in a post-processing script written within Matlab.

After each test, the samples were loaded in the SEM using a more standard holder for high resolution surface imaging, with micrographs of the faces of the pillar taken with a tilt angle of 52°. Engineering stresses and strains were calculated by dividing the applied load by the cross-section area at the mid-height of each pillar and the displacement by the height, respectively (see Fig. 2 (ii)). Note that the uncertainties associated with the cross-sectional area and the height of the pillars were ~2% and ~1% respectively and the magnification of the microscope was verified using a standard sample.

Table 1
Details of nine micropillars fabricated in four different areas (A–D).

Pillar num.	Aspect ratio	Taper angle (°)	Displacement rate (nm/s)	Area	Euler angle(ϕ1,φ,ϕ2)	
					α phase	β phase
1	2.0:1	5.2	5	A	68,14,307	284,35,79
2	1.9:1	6.0	2	B	197,20,157	296,36,30
3	2.2:1	5.4	2			
4	2.2:1	5.3	2			
5	2.1:1	5.4	5			
6	2.2:1	5.4	5			
7	2.0:1	5.6	5			
8	2.6:1	4.4	5	C	20,38,318	302,37,30
9	2.0:1	5.6	5	D	259,68,111	299,35,29

3. Results

3.1. Initial microstructural characterisation

The crystal orientation maps are shown in Fig. 3(i) and (ii), with inserts showing the crystal orientations of α and β phases. The orientations of each region, as described in Table 1, indicate that the *c*-axis of α phase with respect to loading direction varies from 14° (harder grain in region 'A') to 68° (softer grain in region 'D'). Note that the uncertainties associated with absolute crystal

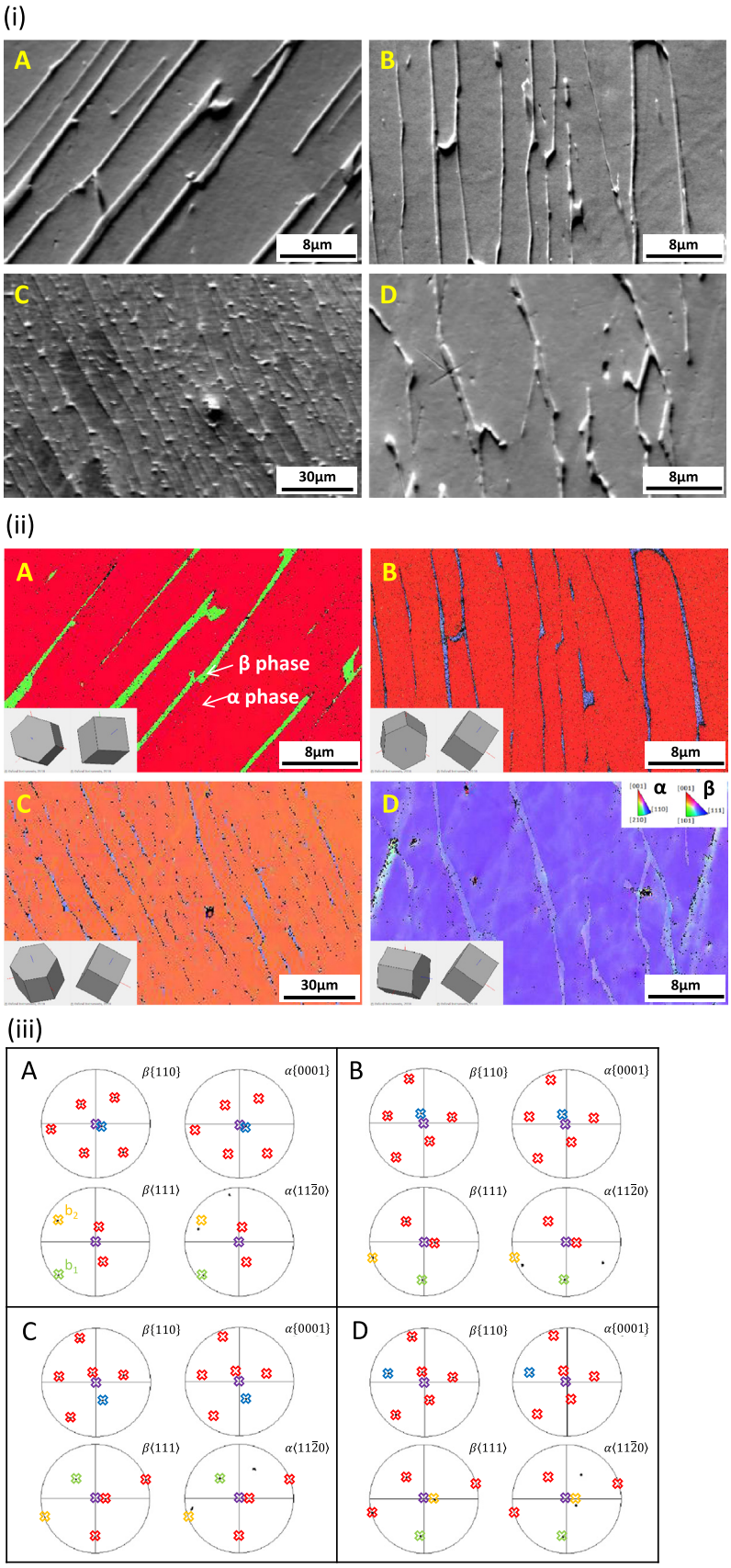

Fig. 3. (i) Secondary electron micrographs and (ii) EBSD derived inverse pole figure (IPF) maps of 4 different regions of interest (ROIs): All maps were taken with respect to normal to the forging direction, and unit cell structures are shown in each ROI, (iii) pole figures of α- and β-Ti in each region, showing overlapping poles in $\{0001\}_\alpha$ and $\{110\}_\beta$ and $\langle 11\bar{2}0\rangle_\alpha$ and $\langle 111\rangle_\beta$, indicating an obedience of Burgers orientation relationship (BOR):the purple cross represents the loading direction. For the direction figures, the green and yellow crosses indicate a_1-/b_1- and a_2-/b_2- directions respectively. For the plane figures the blue crosses represent the shared (0001)//(110) plane. (For interpretation of the references to colour in this, the reader is referred to the web version of this article).

orientation for each each region were within a range of 2° [23]. Furthermore, the related orientations of the α and β phases show that the BOR (Eq. 3) is obeyed within this colony (see overlapping poles in pole figures of each region in Fig. 3(iii)). The morphology of the β ligaments changes subtly in each of the different orientations, with long straight ligaments for the hard-grain orientation, and more wavy and divergent ligaments in the soft grain.

$$\{0001\}_{\alpha} \,//\, \{110\}_{\beta} \text{ and } 11\bar{2}0_{\alpha} \,//\, 111_{\beta} \quad (3)$$

3.2. Effect of α/β morphology

This section outlines mechanical tests of pillars fabricated within the same colony. The pillars were fabricated with an aim of producing tri-crystals with similar internal morphologies, idealised as a vertical 'sandwich' of the thin β ligament between two α crystals, as shown in Fig. 2(i). However, despite best efforts to obtain idealised microstructures, the resultant pillars often have differing internal morphologies.

In Fig. 4 micrographs of nine micropillars before deformation are shown with views taken from the front face (at a tilt angle of 52° in Helios) and back face (at a tilt angle of 30° when mounted on the Alemnis in Auriga). Pillars were fabricated using the same script and have similar dimensions (see Table 1). There are three distinct internal morphologies: sandwich – pillars 2, 4, 7 and 8; minimal β – pillars 1,3 and 9; and mixed α/β – pillars 5 and 6.

Fig. 5 reveals secondary electron micrographs captured during tests and the load–displacement curves for pillars 2–4 and similar mechanical responses are seen for each of these pillars. Each pillar is close to the ideal 'sandwich' morphology. Yield for each pillar occurs at a similar stress value and there are subtle variations in the deformation within the plastic regime.

Fig. 5 also shows highlights from the *in-situ* videos obtained during each test. Typically slip steps formed first within the α phase. Steps in the β phase were observed, but typically these were less strong and therefore harder to observe.

Slip progressed through the pillars, and in P2 the surface slip step was significantly different in the second α crystal, associated with the α/β interface. This is very different to the observation in P4, where slip continued on a similar slip plane in both α crystals.

When the morphology of the β phase is significantly changed, as shown in P5–7 (Fig. 6), the response of the micropillar tri-crystal can be quite significantly different.

In each of these cases, evidence of slip can be seen with surface trace analysis. The slip seems to start in the α crystals but progresses through the pillar quite differently to the response seen in pillars 2–4. P5 and P7 show slip starting towards the top of the pillar, whereas P6 shows slip starting towards the middle of the pillar. Deformation then progressed through the β phase. Deformation of the second α crystal was typically governed by the morphology of the β crystal.

The different surface traces as observed support the significant variations in the load–displacement responses. In particular, pillars 5 and 7 show similar (though subtly different) load–displacement responses whereas pillar 6 shows significantly less hardening and a lower final stress.

3.3. The structurally-affected resolved shear stress

The governing factors to activate slip are the Schmid factor (M), the critical resolved shear stress (CRSS), crystallographic orientation and the loading direction [24]. Orientations from EBSD were used to calculate Schmid factors (with the methodology shown in the Appendix) for $\langle a \rangle$ slip on the basal, prismatic, pyramidal planes and $\langle c + a \rangle$ slip on the pyramidal planes. For $\langle a \rangle$ slip on the basal and prismatic plane these are reported with respect to the Burgers orientation relationship (see Fig. 3(iii)). A table of the Schmid factors for each pillar is shown in Table 2.

Note that among pillars fabricated in region 'B', pillar 7 was chosen to represent this region and furthermore compare its deformation behaviour with pillars in other regions, by minimising the strain rate effect (see Table 1). The anticipated primary slip system and the corresponding maximum Schmid factor (M_{max}) were determined based on previous works that $\langle a \rangle$ slip on the basal and $\langle c + a \rangle$ slip on the 1st order pyramidal plane of α-Ti are typically at room temperature around 20% and 2.3–2.6 times harder to be activated than $\langle a \rangle$ slip on the prismatic slip [6, 25]. These are shown in Table 3 and enable us to anticipate the slip activity such that $\langle a \rangle$ slip on the basal plane would be primarily activated in pillars 1, 7 and 8 and $\langle a \rangle$ slip on the prismatic plane in pillar 9.

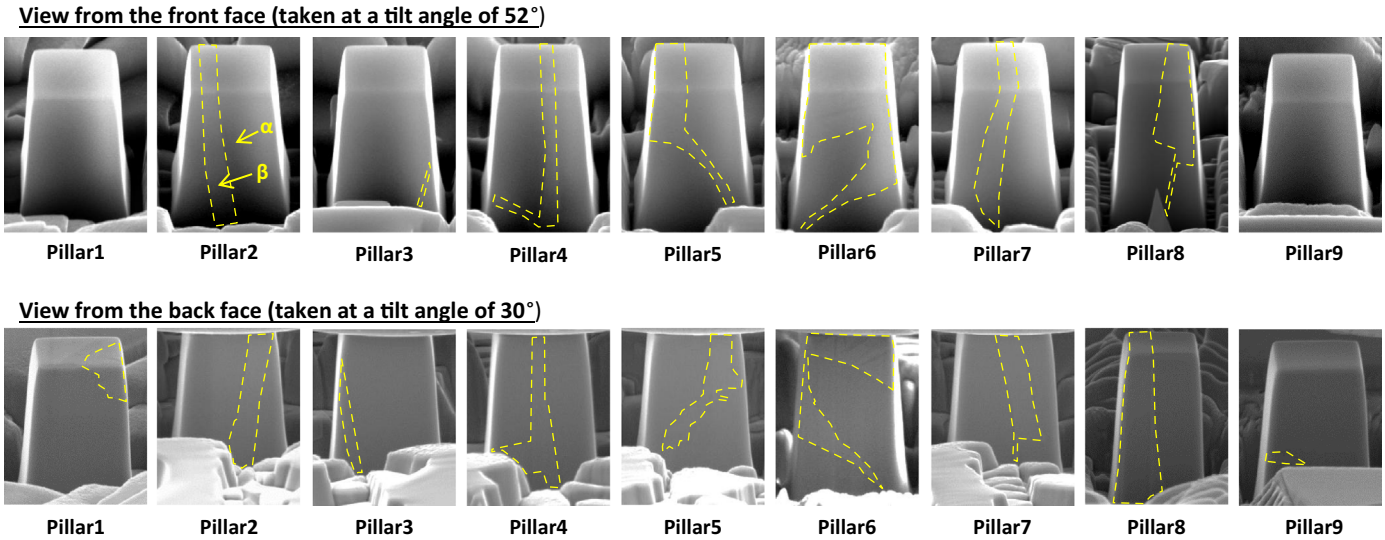

Fig. 4. Micropillars fabricated in region 'A'(pillar 1), 'B'(pillars 2–7), 'C'(pillar 8) and 'D'(pillar 9): All pillars have a top width of 2 μm, and pillar 8 is displayed with different scale due to its higher aspect ratio. Some micrographs showing a view from back face in pillars 1 and 8–9 were observed without indenter tip. β phases within pillars are highlighted with yellow-dash lines. α/β structure can be deduced from the front and back face views (For interpretation of the references to colour in this, the reader is referred to the web version of this article).

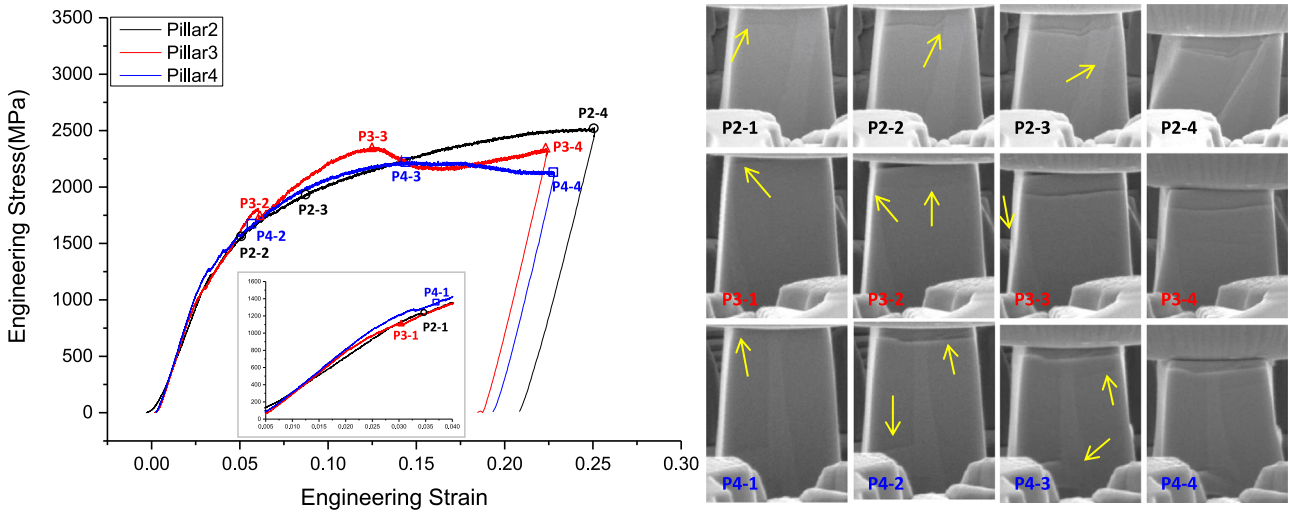

Fig. 5. Engineering stress–strain curves of micropillars 2–4 (fabricated in the same region) with micrographs observed from recorded video: The micrographs were captured at positions marked on the curves. Yellow arrow indicates a main slip occurred at each position (For interpretation of the references to colour in this, the reader is referred to the web version of this article).

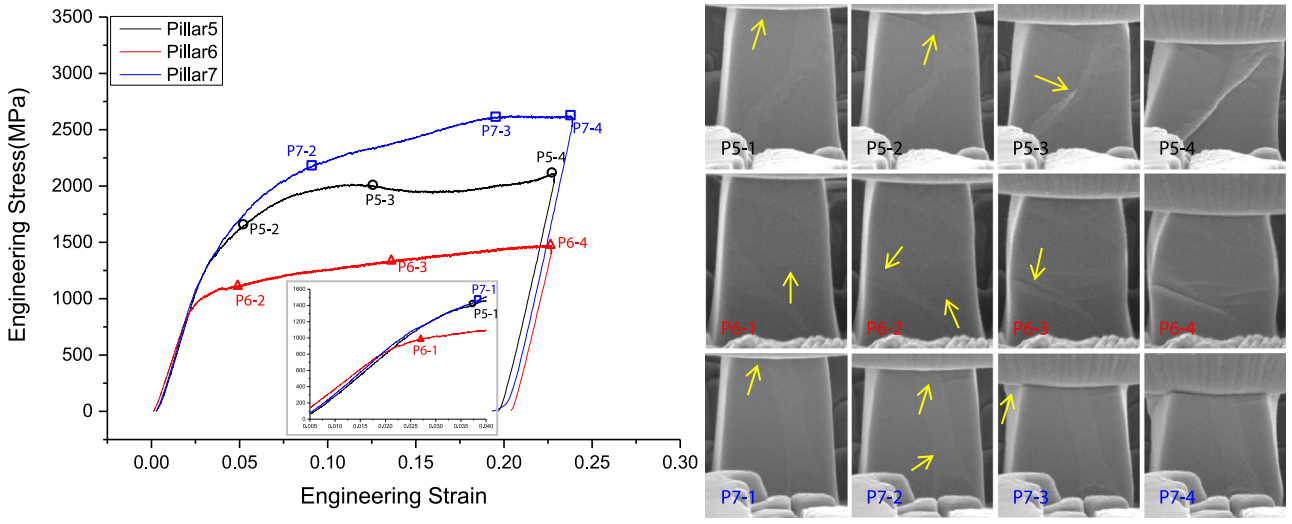

Fig. 6. Engineering stress–strain curves of micropillars 5–7 (fabricated in the same region) with micrographs observed from recorded video: The micrographs were captured at positions marked on the curves. Yellow arrow indicates a main slip occurred at each position (For interpretation of the references to colour in this, the reader is referred to the web version of this article).

Due to the tri-crystal pillar structure, the Schmid factor was then used to determine the structurally-affected resolved shear stress ($\tau_{structure}$) of each pillar using:

$$\tau_{structure} = \sigma_y M_{max} \quad (4)$$

where the yield strength (σ_y) was determined by 0.2% proof stress ($R_{p0.2}$). The offset yield points of each pillar were carefully obtained using stress–strain curves (see Fig. 7) and Table 3 shows the $R_{p0.2}$ and $\tau_{structure}$ values of micropillars 1 and 7–9. It should be noted that interpreting the results is rather difficult due to the non-uniform stress distribution that occurred through the tapered pillar. However, the observed trend is nevertheless informative.

Pillars 1 and 9 are close to single α crystals (see Fig. 4), showing ⟨*a*⟩slip on basal plane has about 23% higher $\tau_{structure}$ (here, close to CRSS) than ⟨*a*⟩ slip on the prismatic plane. This trend is similar to those typically found in the literature [6, 25]. Pillars 7 and 8 have lower $\tau_{structure}$ than pillar 1, although their slip activities were similarly anticipated. This is likely experienced by the effect of structural morphology within the pillars. More details are discussed in the next section.

4. Discussion

The significant anisotropic behaviour of the α phase at the single grain crystallite level is well-known and directly related to elastic properties (i.e., stiffness) and plastic deformation (i.e., slip resistance on different crystallographic planes). This indicates that not only are mechanical properties within grains highly dependent on their crystallographic orientation, but the deformation mechanism is strongly localised even at the macroscopic level. Micropillar compression testing with the aid of SEM/EBSD, FIB and nanoindenter (Alemnis) has been demonstrated to offer huge potential as an effective technique in investigating micromechanics of two-phase Ti alloys and other materials.

Micropillars with square cross-section were machined to simplify slip trace analysis. This geometry has its drawback, as square shape pillars may have a higher strain hardening and earlier strain bursts compared to cylindrical geometry [26]. However, the aim of the present study is not to obtain precise mechanical properties but to find the morphological effects of α/β phases and phenomenological observation of local deformation with differently activated slip systems.

Table 2
Schmid factors of HCP α phase (30 slip systems in total).

		Slip system	P1	P7	P8	P9		Slip system	P1	P7	P8	P9
⟨a⟩ Basal	⟨a_1⟩	(0001)[$\bar{2}$110]	**0.23**	0.26	**0.46**	0.34	⟨c + a⟩ Pyram.(1st)	($\bar{1}$011)[2$\bar{1}\bar{1}$3]	0.44	0.31	0.26	0.47
	⟨a_2⟩	(0001)[1$\bar{2}$10]	0.14	**0.30**	0.36	0.12		(0$\bar{1}$11)[11$\bar{2}$3]	0.34	0.49	0.13	0.03
	⟨a_3⟩	(0001)[11$\bar{2}$0]	0.09	0.04	0.10	0.22		(1$\bar{1}$01)[$\bar{1}$2$\bar{1}$3]	0.24	0.47	0.14	0.11
⟨a⟩ Prism	⟨a_1⟩	(01$\bar{1}$0)[$\bar{2}$110]	0.01	0.06	0.11	0.13		(10$\bar{1}$1)[$\bar{1}\bar{1}$23]	0.26	0.46	0.01	0.01
	⟨a_2⟩	(10$\bar{1}$0)[$\bar{1}$2$\bar{1}$0]	0.03	0.04	0.19	0.29		(01$\bar{1}$1)[1$\bar{2}$13]	0.37	0.26	0.23	0.15
	⟨a_3⟩	($\bar{1}$100)[$\bar{1}\bar{1}$20]	0.02	0.01	0.08	**0.42**		($\bar{1}$101)[2$\bar{1}\bar{1}$3]	0.46	0.14	0.32	0.37
⟨a⟩ Pyram.		(10$\bar{1}$1)[$\bar{1}$2$\bar{1}$0]	0.04	0.18	0.01	0.31		($\bar{1}$011)[11$\bar{2}$3]	0.49	0.26	0.44	0.37
		(01$\bar{1}$1)[$\bar{2}$110]	0.12	0.07	0.32	0.28		(0$\bar{1}$11)[$\bar{1}$2$\bar{1}$3]	0.39	0.40	0.19	0.01
		($\bar{1}$101)[$\bar{1}\bar{1}$20]	0.06	0.01	0.12	0.27		(1$\bar{1}$01)[$\bar{2}$113]	0.26	0.49	0.15	0.14
		($\bar{1}$011)[1$\bar{2}$10]	0.09	0.11	0.34	0.19	⟨c + a⟩ Pyram.(2nd)	(11$\bar{2}$2)[$\bar{1}\bar{1}$23]	0.38	0.38	0.23	0.00
		(0$\bar{1}$11)[2$\bar{1}\bar{1}$0]	0.11	0.17	0.12	0.05		($\bar{1}$2$\bar{1}$2)[1$\bar{2}$13]	0.48	0.23	0.34	0.04
		(1$\bar{1}$01)[11$\bar{2}$0]	0.03	0.03	0.02	0.47		($\bar{2}$112)[2$\bar{1}\bar{1}$3]	0.50	0.25	0.33	0.46
⟨c + a⟩ Pyram.(1st)		(10$\bar{1}$1)[$\bar{2}$113]	0.28	0.37	0.02	0.16		($\bar{1}\bar{1}$22)[11$\bar{2}$3]	0.46	0.41	0.32	0.19
		(01$\bar{1}$1)[$\bar{1}\bar{1}$23]	0.43	0.22	0.40	0.00		(1$\bar{2}$12)[$\bar{1}$2$\bar{1}$3]	0.35	0.48	0.03	0.07
		($\bar{1}$101)[1$\bar{2}$13]	0.49	0.15	0.38	0.22		(2$\bar{1}\bar{1}$2)[$\bar{2}$113]	0.30	0.48	0.07	0.17

Table 3
0.2% proof stress ($R_{p0.2}$) and the structurally-affected resolved shear stress ($\tau_{structure}$) determined in micropillars 1 and 7–9.

	P1	P7	P8	P9
Primary slip	⟨a_1⟩ Basal	⟨a_2⟩ Basal	⟨a_1⟩ Basal	⟨a_3⟩ Prism
M_{max}	0.23	0.30	0.46	0.42
$R_{p0.2}$ (MPa)	1745 (±36)	1180 (±22)	640 (±12)	779 (±14)
$\tau_{structure}$ (MPa)	401 (±8)	354 (±7)	294 (±6)	327 (±6)

An important aspect regarding the morphological effect is shown in Figs. 5 and 6. Strain rates were similar for pillars 2–4 ($4.5–5.1 \times 10^{-4}\,s^{-1}$) and 5–7 ($1.1–1.2 \times 10^{-3}\,s^{-1}$) and hence the rate effects were minimised. Note, however, that we only considered here the α/β morphology and it is thought that the volume fraction of each phase may also have some effects on local deformation. Interestingly, in pillars 2–7 all slip steps formed first within the α phase, mostly toward the top of the pillar except pillar 6 showing slip starting towards the middle. The mechanistic basis for this phenomenon remains elusive, because the slip steps only indicate the out of pillar slip events and do not necessarily reflect the in-pillar deformation. It may be conjectured that this is either due to different dislocation evolution mechanism of each phase and the associated slip system or difference of phase properties. The figures also show that yield points vary through pillar morphologies and hardening behaviours are quite different, particularly in pillar 5 and 6 (mixed α/β), resulting in quite different stress–strain response in plastic regime. The results suggest that it might be argued that similar β morphologies lead to similar stress–strain response in the elastic and early plastic regimes.

Local slip activities with respect to crystal orientations were studied with pillars 1 and 7–9. The pillars have sandwich or

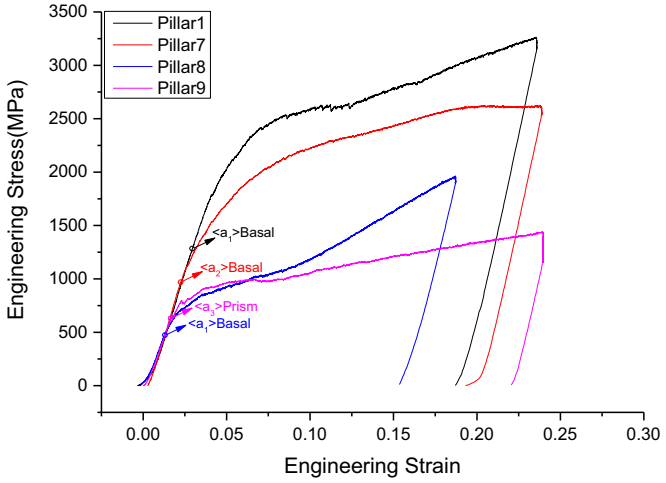

Fig. 7. Engineering stress–strain curves of micropillars 1 and 7–9, all fabricated in different regions (harder grain toward pillar 1 and softer toward pillar 9): Open circles marked on the curves indicate the 'yield' points observed for each pillar, and the corresponding primary slip system activated also noted.

minimal β structures, which may be less affected by structural morphologies. In the previous section, the primary slip system of each pillar was anticipated. Possible slip on HCP crystals at room temperature is described as ⟨a⟩ slip on the basal plane ⟨11$\bar{2}$0⟩{0001}, the prismatic plane ⟨11$\bar{2}$0⟩{10$\bar{1}$0}, the pyramidal plane ⟨11$\bar{2}$0⟩{10$\bar{1}$1} and ⟨c + a⟩ slip on the planes ⟨11$\bar{2}$3⟩{10$\bar{1}$1} and ⟨11$\bar{2}$3⟩{11$\bar{2}$2}.

Fig. 8 shows the SE micrographs of deformed pillars 1 and 7–9, and the associated unit cell structures. Loading directions for unit

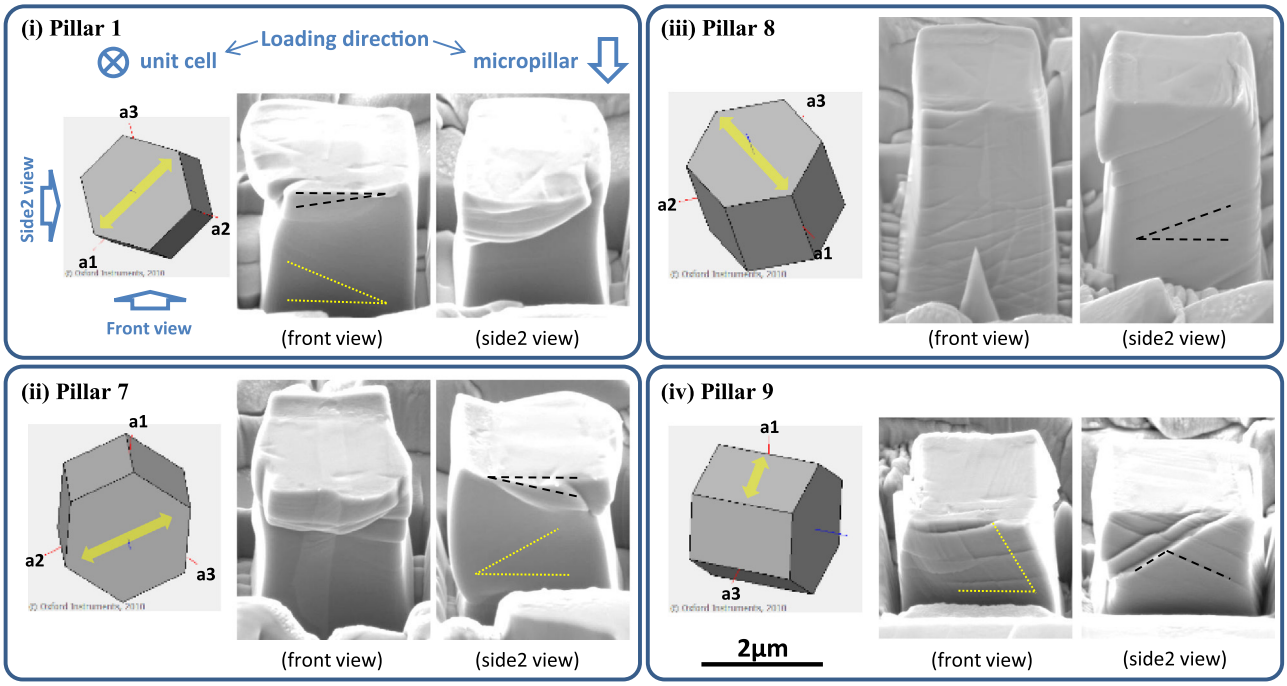

Fig. 8. SEM micrographs of the deformed micropillars (i) 1, (ii) 7, (iii) 8 and (iv) 9, observed views from the front and side2 faces at the tilt angle of 52°: Consider that the loading directions of HCP unit cells and pillar micrographs are out of plane and vertical direction, respectively. The double-arrow in yellow indicates the anticipated primary slip direction, the dash line in black indicates the resultant primary slip angle and the dot line in yellow indicates the resultant secondary slip angle (For interpretation of the references to colour in this, the reader is referred to the web version of this article).

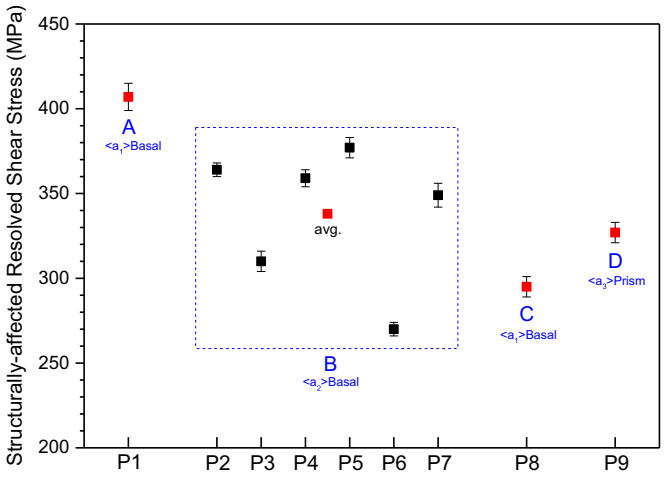

Fig. 9. Distribution of the structurally-affected resolved shear stress ($\tau_{structure}$) determined for micropillars 1–9.

cell and pillars are out of plane and vertical, respectively. The a_1-, a_2- and a_3-directions of HCP crystals were determined based on the BOR analysis shown in Fig. 3(iii). The yellow-double arrow on the unit cell indicates the primary slip direction anticipated from the Schmid factor calculation. It is seen in the micrographs of front and side2 views that all pillars deformed following the anticipated primary slip plane and direction. The slip angles caused by the primary slip (see the black dashed line on pillars) are approximately 13.1° (pillar 1), 19.5° (pillar 7), 25° (pillar 8) and 123° (pillar 9). Not surprisingly the angles are similar to the angle γ, between the *c*-axis of a crystal and loading direction, 14° for pillar 1 and 20° for pillar 7, except for pillar 8 (38°) due to significant angle changes during deformation. The secondary slip can be seen in the micrographs and the angles were indicated with yellow-dot line. In pillars 1 and 7, it might be thought that $\langle c+a \rangle$ slip on the pyramidal plane was activated, although at this stage it is difficult to confirm the corresponding slip system and further investigation is required. $\langle a \rangle$ slip on the basal plane was found in pillar 9, with the slip angle of approximately 66° which is well matched with the angle γ of 68°.

Schmid's law enables the reasonable prediction of the primary and further secondary slip activities through various crystal orientations within localised areas. However, it should be noted that Schmid's law can be ineffective when the β structure varies significantly. Fig. 9 reveals $\tau_{structure}$ variations determined for all the micropillars studied. $\tau_{structure}$ values vary through pillars 2–7, all of which were fabricated in region 'B'. Particular difference is found in both P3 and P6; the former shows an earlier α/β phase interaction than other (see Fig. 5), and the latter shows a quite different β morphology to others (see Fig. 6). This suggests that structural morphology is a sensitive trigger of material yielding within localised areas.

5. Conclusions

In the present paper, micromechanical testing using a micropillar compression technique was carried out in order to investigate the local deformation mechanisms of two-phase Ti alloy. The elastic and plastic anisotropy inherent to α crystal leads to significant inhomogeneity in stress and strain at the microstructural level. In addition, interaction between α and β crystal gives rise to a complex interplay of morphological and orientation relationship. It is therefore insightful to demonstrate local deformation mechanisms by testing local mechanical responses within isolated morphologies.

A total of nine micropillars were fabricated in four determined regions, each of which has distinct α crystal orientations. Euler angles of each phase were effectively obtained with EBSD measurements and subsequently used to calculate the Schmid factor. The main findings are summarised as:

1. It is shown that a combination of SEM/EBSD, FIB and *in-situ* deformation with a nanoindenter (Alemnis) are effective tools to investigate micromechanical deformation of two-phase Ti alloys and potentially other materials.
2. The structurally-affected resolved shear stress ($\tau_{structure}$) was determined based on experimental observations. In pillars with near α crystal structure, ⟨*a*⟩ slip on basal planes gives about 23% higher $\tau_{structure}$ (here, close to CRSS) than ⟨*a*⟩ slip on prismatic planes, which is typically found in the literature.
3. We found that local slip activities were in general anticipated by Schmid's law, though it became ineffective when β structure significantly changed. This indicates that structural morphology highly affects material yielding within a localised area.
4. Morphology of the α/β phases has significant effect on local deformation behaviour: (1) similar β morphology and similar α slip systems lead to similar stress–strain response, yet the effect of β volume fraction is not clear; (2) the β structure (or shape) within a pillar significantly affect the stress–strain response and the maximum stress level. The findings suggest the need for further investigations by testing pillars of similar morphology to confine morphological effects.
5. The advantage of micropillar compression is to obtain information of (unconstrained) mechanical properties at small volumes. This provides a basis from which to investigate grain-to-grain (e.g., slip transfer) and phase-to-phase (e.g., dislocation density evolution at phase interface) interactions, which are not yet understood.

Acknowledgement

We appreciate helpful discussions with Dr Finn Giuliani concerning micromechanical deformation methods. We are grateful to the Engineering and Physical Science Research Council for funding through HexMat (EP/K034332/1). Further details of the HexMat grant can be found at http://www.imperial.ac.uk/hexmat. TBB would like to thank the Royal Academy of Engineering for funding his Research Fellowship.

Appendix A. Supplementary material

Supplementary data associated with this article can be found in the online version at doi:10.1016/j.msea.2015.09.016.

Appendix. . Calculation of Schmid factors

In order to obtain the Schmid factor of the α phase, a script written within Matlab was used to calculate the values for all 30 slip systems (see Table 2). It should be aware that the reference unit cell coordinates vary according to an instrument being used. In Bruker EBSD system, the *c*-axis is aligned with the crystal *z*-axis and a_2-axis with the crystal *y*-axis. This gives a 'basis matrix (*abc*)' and a 'reciprocal basis matrix (abc^*)' as follows:

$$abc = \begin{bmatrix} 0.2555 & 0 & 0 \\ -0.1475 & 0.2950 & 0 \\ 0 & 0 & 0.4680 \end{bmatrix} and\ abc^* = \begin{bmatrix} 3.9139 & 1.9569 & 0 \\ 0 & 3.3898 & 0 \\ 0 & 0 & 2.1368 \end{bmatrix} \quad (5)$$

where lattice constants of HCP Ti used here are $a=0.295$ nm and $c=0.468$ nm. For a direction [*uvtw*] and plane (*hkil*), i.e., using 4 index notations, Hexagonal vectors were transferred to the Cartesian vectors with following relations:

$$\begin{matrix} u \\ v \\ w \end{matrix}_{Cartesian} = \begin{matrix} 2u+v \\ 2v+u \\ w \end{matrix}_{Hexagonal} \times abc \quad (6)$$

$$\begin{matrix} h \\ k \\ l \end{matrix}_{Cartesian} = \begin{matrix} h \\ k \\ l \end{matrix}_{Hexagonal} \times abc^* \quad (7)$$

where $2u+v$ and $2v+u$ come from using the redundant index for a lattice direction.

A slip direction and slip plane normal were then obtained using 30 slip systems in Cartesian vectors with the following rotation matrix (*g*):

$$g = \begin{bmatrix} c\varphi_1 c\varphi_2 - c\Phi s\varphi_1 s\varphi_2 & c\varphi_2 s\varphi_1 + c\varphi_1 c\Phi s\varphi_2 & s\Phi s\varphi_2 \\ -c\varphi_1 s\varphi_2 - c\Phi c\varphi_2 s\varphi_1 & c\varphi_1 c\Phi c\varphi_2 - s\varphi_1 s\varphi_2 & c\varphi_2 s\Phi \\ s\varphi_1 s\Phi & -c\varphi_1 s\Phi & c\Phi \end{bmatrix} \quad (8)$$

where the Euler angles φ_1, ϕ, φ_2 were obtained from the EBSD measurement and *c* and *s* indicate cosine and sine of each angle, respectively. The Schmid factor was then achieved by the following equation:

$$M = \cos\phi \cos\lambda = (l \cdot s)(l \cdot n) \quad (9)$$

where ϕ is the angle between slip plane normal (n) and loading direction (l), and λ is the angle between loading direction and slip direction (s). Note that we only considered the Schmid factor of α phase due to the fact that β orientations in areas 'B', 'C' and 'D' were about the same (see Table 1) and pillar 1 in area 'A' has minimal β phase on the top corner of the pillar. This leads to the assumption that all pillars have little or similar orientation effect of β phase on deformation.

References

[1] F.P.E. Dunne, D. Rugg, Fatigue Fract. Eng. Mater. Struct. 31 (2008) 949–958.
[2] P. Partridge, Int. Mater. Rev. (1967) 169–194.
[3] N. Paton, J. Williams, G. Rauscher, The deformation of α-phase titanium, Titanium Science and Technology, Plenum Press (1973), p. 1049–1069.
[4] M. Savage, J. Tatalovich, M. Zupan, K. Hemker, M. Mills, Mater. Sci. Eng.: A 319 (2001) 398–403.
[5] J. Williams, R. Baggerly, N. Paton, Metall. Mater. Trans. A 33 (2002) 837–850.
[6] J. Gong, A.J. Wilkinson, Acta Mater. 57 (2009) 5693–5705.
[7] J. Gong, A.J. Wilkinson, Acta Mater. 59 (2011) 5970–5981.
[8] K. Chan, C. Wojcik, D. Koss, Metall. Trans. A 12 (1981) 1899–1907.
[9] J. Qiu, Y. Ma, J. Lei, Y. Liu, A. Huang, D. Rugg, R. Yang, Metall. Mater. Trans. A 45 (2014) 6075–6087.
[10] R.S.Sandala, University of Manchester, 2012.
[11] M. Savage, J. Tatalovich, M. Mills, Philos. Mag. 84 (2004) 1127–1154.
[12] S. Suri, G. Viswanathan, T. Neeraj, D.-H. Hou, M. Mills, Acta Mater. 47 (1999) 1019–1034.
[13] M.D. Uchic, D.M. Dimiduk, J.N. Florando, W.D. Nix, Science 305 (2004) 986–989.
[14] J.R. Greer, J.T.M. De Hosson, Prog. Mater. Sci. 56 (2011) 654–724.
[15] D. Dimiduk, M. Uchic, T. Parthasarathy, Acta Mater. 53 (2005) 4065–4077.
[16] J.A. El-Awady, M.D. Uchic, P.A. Shade, S.-L. Kim, S.I. Rao, D.M. Dimiduk, C. Woodward, Scr. Mater. 68 (2013) 207–210.
[17] D. Kiener, P. Guruprasad, S. Keralavarma, G. Dehm, A. Benzerga, Acta Mater. 59 (2011) 3825–3840.
[18] Q. Sun, Q. Guo, X. Yao, L. Xiao, J.R. Greer, J. Sun, Scr. Mater. 65 (2011) 473–476.
[19] Q. Yu, Z.-W. Shan, J. Li, X. Huang, L. Xiao, J. Sun, E. Ma, Nature 463 (2010) 335–338.
[20] R. Ding, J. Gong, A.J. Wilkinson, I.P. Jones, Philos. Mag. 92 (2012) 3290–3314.
[21] I. Jones, W. Hutchinson, Acta Metall. 29 (1981) 951–968.
[22] C. Volkert, A. Minor, MRS Bull. 32 (2007) 389–399.
[23] G. Nolze, Ultramicroscopy 107 (2007) 172–183.
[24] E. Tenckhoff, Deformation Mechanisms, Texture, and Anisotropy in Zirconium and Zircaloy, Special Technical Publication 966. ASTM, Philadelphia, PA, 1988.
[25] G.Lutjering, J.C.Williams, Springer, New York, (2007).
[26] G. seok Kim, Université de Grenoble, 2011.